Video-Based Measuring of Quality Parameters for Tricuspid Xenograft Heart Valve Implants

Alexandru Paul Condurache*, Tobias Hahn, Michael Scharfschwerdt, Alfred Mertins, *Senior Member, IEEE*, and Til Aach, *Senior Member, IEEE*

***Abstract*—Defective heart valves are often replaced by implants in open-heart surgery. Both mechanical and biological implants are available. Among biological implants, xenograft ones—i.e., valves grafted from animals such as pigs, are widely used. Good implants should exhibit certain typical anatomical and functional characteristics to successfully replace the native tissue. Here, we describe a video-based system for measuring quality parameters of xenograft heart valve implants, including the area of the orifice and the fluttering of the valves' leaflets, i.e., their flaps (or cusps). Our system employs automatic methods that provide a precise and reproducible way to infer the quality of an implant. The automatic analysis of both a valve's orifice and the fluttering of its leaflets offers a more comprehensive quality assessment than current, mostly manual methods. We focus on valves with three leaflets, i.e., aortic, pulmonary, and tricuspid valves.**

***Index Terms*—Fluttering quantification, heart valve implants, image analysis, quality measures.**

I. Introduction

DEFICIENT and malfunctioning heart valves must be often replaced in open-heart surgery to prevent a severe deterioration of the patient's health. Since 1996, there have been some 60 000 such interventions in the U.S. each year [25]. Clearly, there is a major interest in the quality of these implants as this is directly related to their life span and the occurrence of complications for the patient.

Since 1950, some 80 types of implants have been developed, comprising both mechanical and biological implants. Here, we focus on biological ones. Depending on their origin, biological implants are of three types: *xenograft implants*, which consist of similar tissue collected from specially bred animals, most often pigs; *homograft implants*, which consist of tissue from a deceased person; and *autograft implants*, where, e.g., a patient's own pulmonary valve is used to replace the aortic valve and another—usually homograft—implant replaces the pulmonary valve. Xenograft implants are the most often used biological implants. Biological implants can be distinguished into two different types: *stented implants*, where the valve is placed on a support frame and *stentless implants*, without the support frame [6], [24]. Examples are shown in Fig. 1. A normal human heart has both valves with two and three leaflets. The valve in Fig. 1(b) is a three-leaflet xenograft stentless implant and one of those analyzed in this paper.

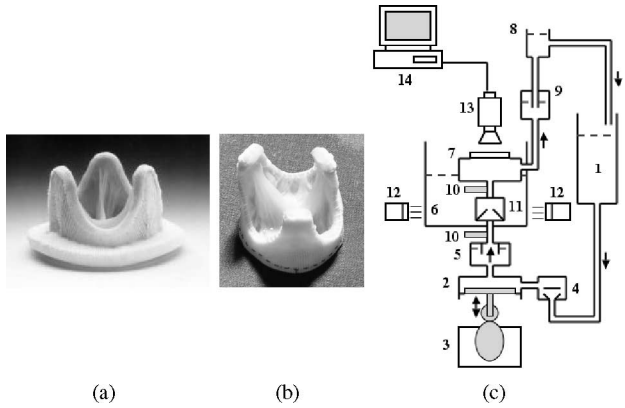

Fig. 1. (a) Stented xenograft implant, (b) stentless xenograft implant, and (c) the diagram of our test setup.

Medical studies show that implants do not by far reach the reliability of native valves, mainly because they do not have the autorepair abilities of native tissue. Thus, complications reappear often after a certain period of time, eventually making a new intervention necessary. To ensure that only the best implants reach the patients, their characteristics are verified before they are implanted.

There are two major quality criteria that characterize a heart valve implant [7], [19], [20], [23].

1) *The time-dependent area of the orifice* from the moment the valve opens until it closes. Here, we call the function of orifice area over time *the orifice curve*. An orifice curve is shown in Fig. 2.
2) *The fluttering* of the leaflets in the blood flow (see Fig. 3).

The quality of a valve is evaluated using a video sequence showing an entire *valve cycle*, i.e., the time interval from the moment the valve starts opening until it is completely closed. We call such a movie a *test sequence*. Imaging is done by means of a special test setup [23] shown in Fig. 1(c). From a reservoir (1), a transparent fluid—usually water, which with respect to the investigated valve properties behaves similarly to blood—is transported through a disc valve (4) by a piston pump (2), which is driven by a waveform-adapted cam plate (3). After passing an input compliance (5), the fluid is pressed through

Manuscript received October 17, 2007; revised April 19, 2008. First published June 20, 2008; current version published November 20, 2009. *Asterisk indicates corresponding author.*

*A. P. Condurache is with the Institute for Signal Processing, University of Lübeck, D-23538 Lübeck, Germany (alexandru.condurache@isip.uni-luebeck.de).

T. Hahn was with the Institute for Signal Processing, University of Lübeck, D-23538 Lübeck, Germany. He is now with the Department for Software Quality Assurance, Siemens Medical Solutions, D-90152 Erlangen, Germany.

M. Scharfschwerdt is with the Clinic for Heart Surgery, University Clinic Schleswig-Holstein, D-23538 Lübeck, Germany.

A. Mertins is with the Institute for Signal Processing, University of Lübeck, D-23538 Lübeck, Germany.

T. Aach is with the Institute of Imaging and Computer Vision, Rheinisch-Westfaelische Technische Hochschule (RWTH) Aachen University, D-52056 Aachen, Germany.

Digital Object Identifier 10.1109/TBME.2008.2001290

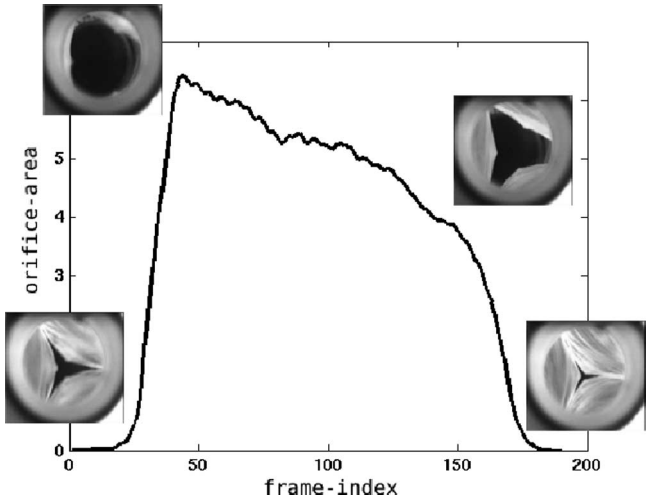

Fig. 2. Orifice curve showing the evolution of the orifice area over the frame index in a test sequence.

the inspected heart valve (11) into a visualization chamber (7) located in another fluid reservoir (6). Pressure sensors (10) are installed below and above the heart valve. Passing an aortic compliance (9), the fluid reaches a vertical pipe of variable length and flows back to the first reservoir. The heart valve is illuminated by light sources (12) placed outside the fluid tank (6), which is made from perspex. A black and white video camera (13) takes images of the heart valve with 500 f/s and a resolution of 480×420 pixels. The digitized images are stored in a PC (14). Usually, a test sequence (see Fig. 2) has a duration of some half a second, leading to approximately 250 frames.

Currently, for quality assessment, the orifice curve is measured manually [23]. To compute the opening area of a tricuspid heart valve, the human operator has to mark the points at the connections between leaflets and at the peak of each leaflet. Also, by including the midpoint of the opening, one can define six triangles that approximate the area of the orifice of a three-leaflet valve. For each analyzed heart valve, this procedure, which neglects the rather curved boundary of the leaflets, has to be repeated for some images properly chosen over the test sequence. From these measurements, the orifice curve is interpolated and the behavior of the implant is inferred. Even for only a few images, this is a rather tedious job, and it clearly returns imprecise results because it does not consider the entire sequence.

During a typical test run, the fluttering is analyzed only visually by the operator if at all. In some special cases—related to medical research rather than medical routine—the fluttering is also analyzed. For this purpose, the bending deformation index (BDI) [7] is again manually computed only for a few images. The BDI is computed as the depth of a leaflet's border divided by its side [see Fig. 3(b)].

Here, we introduce novel methods for machine-vision-based support of the quality assessment of xenograft heart valve implants. We show how to measure the orifice area and the fluttering of the leaflets automatically. This will allow for an improved human-based quality control, as these measurements are more

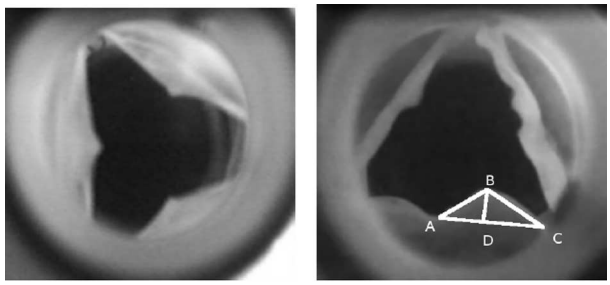

(a) (b)

Fig. 3. Examples of valves. (a) Without fluttering. (b) With fluttering. For the fluttering valve, the BDI is computed as $|\overline{BD}|/|\overline{BC}|$.

precise and reproducible. Also, an analysis of fluttering becomes available in medical routine now. Such measurements may also represent the basis for fully automated analysis, which can be conducted fast and for a large number of valves, which is clearly interesting for companies producing such implants. This study draws on previously published conference papers [4], [10], but additionally describes more recent results for an extended analysis of fluttering.

II. Measuring Orifice Area

To obtain an orifice curve, the orifice needs to be segmented in each image of a test sequence. In our test setup, the orifice appears dark when the valve opens, while the valve itself is bright. Therefore, a straightforward approach to segmentation is thresholding [10]. However, threshold-based methods usually fail because the orifice does not exhibit sufficiently homogeneous gray levels. The orifice is defined by the borders of the leaflets, it is transparent, and it will thus assume the gray levels of the structures against which it is imaged. Practice shows that it is rather difficult to achieve a homogeneous background to project the orifice against.

For a better segmentation, one should thus start from the leaflets and select the orifice as defined by their borders—i.e., as the area enclosed within these borders. The border-shaped curves cannot be described *a priori* as they have a large variability, therefore snakes [15] and related techniques [3], [17] are well-suited to track them over the analyzed sequence [4]. For our purposes, the use of the standard snakes as introduced in [15] appears perfectly justified, because we do not encounter any changes in the topology of the sought boundary curve—neither over time for a given valve nor over different valves—as there is always only one orifice to segment in each analyzed image.

A. Orifice Segmentation by Snakes

Active contours or snakes are highly adaptable models and therefore widely used in the analysis of medical images [18], [22], [28]. A snake is a curve $\mathbf{v}(s) = [x(s), y(s)]$, $s \in [0, 1]$, evolving over the spatial domain of an image under the influence of forces derived from internal and external energy terms to a position of minimum energy.

The internal energy term E_{int} governs the behavior of the snake during its evolution. It is defined such that it penalizes stretching and bending, thus encouraging smooth solutions

$$E_{\text{int}} = \int_0^1 \frac{1}{2}\left(\alpha(s)\left|\frac{\partial \mathbf{v}(s)}{\partial s}\right|^2 + \beta(s)\left|\frac{\partial^2 \mathbf{v}(s)}{\partial s^2}\right|^2\right) ds. \quad (1)$$

The first-order term controls stretching and the second-order term bending. The weights $\alpha(s)$ and $\beta(s)$ adjust the influence of the two terms and thus favor a specific snake behavior. We have chosen them to be constant over the snake: $\alpha(s) = \alpha$ and $\beta(s) = \beta$.

The external energy term E_{ext} is computed from the image such that it reaches a minimum over the sought image features

$$E_{\text{ext}} = \int_0^1 P(\mathbf{v}(s))ds \quad (2)$$

where the potential energy function $P(x(s), y(s))$ can be specified as

$$P(x, y) = -|\nabla(g_\sigma(x, y) * i(x, y))|^2 \quad (3)$$

to attract the snake toward edges. In this case, $g_\sigma(x, y)$ is a 2-D Gaussian kernel, which is convolved with the image $i(x, y)$ to extend the attraction range of the edges.

The snake energy functional can then be written as $E = E_{\text{int}} + E_{\text{ext}}$. The snake will evolve to a position where E is at least locally minimized. The minimization problem is solved by setting to zero the corresponding Euler–Lagrange equation. Thus, one obtains the force formulation of a snake: $F_{\text{int}} + F_{\text{ext}} = 0$.

As an external force for the snake, we use a gradient vector flow (GVF) [26], [27], which has an improved attraction range and concavity behavior in comparison to other external forces [14]. A GVF $\mathbf{G}(x, y) = (u(x, y), v(x, y))$ is a static external force field. If $f(x, y) = -P(x, y)$, then $\mathbf{G}$ is defined as the vector field that minimizes the energy functional

$$\mathcal{F} = \iint \mu\left(\left(\frac{\partial u}{\partial x}\right)^2 + \left(\frac{\partial u}{\partial y}\right)^2 + \left(\frac{\partial v}{\partial x}\right)^2 + \left(\frac{\partial v}{\partial y}\right)^2\right) dxdy + \iint |\nabla f|^2 |\mathbf{G} - \nabla f|^2 dxdy \quad (4)$$

with μ being a parameter. Consequently, $\mathbf{G}$ is equal to $-\nabla P(x, y)$ when $|\nabla P(x, y)|$ is large. Otherwise, it is governed by its own partial derivatives, thus discouraging abrupt changes in the external energy and forcing the field to be slowly varying in homogeneous regions, thereby greatly extending the attraction range. The optimal position of the snake is sought by gradient descent methods.

The snake has to be initialized automatically and only after the valve has opened wide enough for the orifice to appear. We define leaflet *baselines* as the lines connecting each of the *anchor points*. Anchor points are the points where two leaflets meet [see Fig. 4(a)]. Baselines and anchor points are estimated automatically. We initialize the snake from the base lines. After initialization, the snake will track the outline of the leaflets until the valve is almost closed.

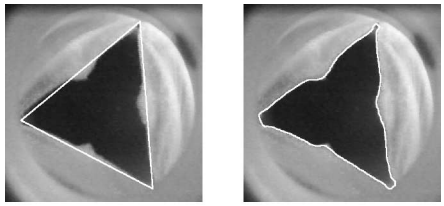

(a) (b)

Fig. 4. (a) Initialization of the snake from the baselines. (b) Result after convergence was achieved.

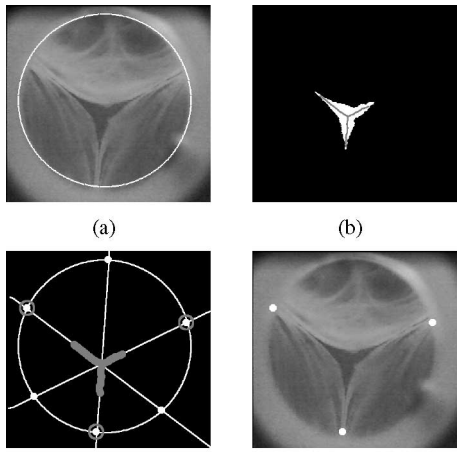

(a) (b) (c) (d)

Fig. 5. Automatic detection of anchor points: (a) original image with overlay of the detected circular outline, (b) segmented orifice with centerlines (in dark gray), (c) centerlines (thick dark gray), centerline rays (thin white), their intersections with the circular outline (white points), and minimum-distance points (with dark gray circle) computed as those intersection points closest to the centerlines, and (d) final result.

1) Segmentation of Supportive Image Items: To ensure a successful segmentation of the orifice, we have adapted our algorithms to explicitly use available prior knowledge. Toward this end, we segment several image items: the *circular outline* of the valve and the anchor points of the leaflets.

a) Segmentation of circular outline: The camera observes the valve through a cylindrical tube using a normal imaging optical system [13]. Thus, the inner wall of the tube is also observable and delineates the contour of the valve. We call this the circular outline of the valve.

We segment the circular outline by the Hough transform for circles [11], [12] on the image obtained after edge detection [2]. As the approximate position of the center of this circle and the approximate size of its radius are known *a priori*, the search in the Hough space is very fast. We search the coordinates of the center in a region of interest (ROI) of size 15 pixels centered at the image center and the radius on an interval of the same size centered at the value 150. The center and radius of the outline circle are then estimated by taking the mean over several images. This defines a circular ROI where only the valve is visible. An example is shown in Fig. 5(a).

b) Automatic determination of anchor points: To find the anchor points, we use the first 11 frames after the valve has opened, but before the valve is completely open. For these

images, we can safely assume that the orifice is sufficiently small to exhibit a narrow and specific gray level representation to segment it by thresholding. One such example is shown in Fig. 5(a) and the corresponding segmentation is depicted in Fig. 5(b).

To find the lines where each two leaflets meet (called centerlines in the following), the orifice-segmentation result is dilated and then thinned using a circular structuring element. The dilation is necessary to eliminate artifacts at the borders of the segmented orifice, such that only the centerlines remain after thinning. The centerlines are shown in dark gray in Fig. 5(b). The centerlines are used to extrapolate the centerline rays by means of the Hough transform for lines. The centerline rays are shown in white in Fig. 5(c). For each centerline ray in image m (with $m = 1, \ldots, 11$), we then find the points where it intersects the circular outline. Subsequently, the distances from each intersection point to all centerline points along the corresponding ray are computed and only the minimum distance is considered. We thus have two such minima per ray. An anchor point $\mathbf{x}^m_{\mathrm{AP}_i}$, corresponding to the ith centerline ($i = 1, \ldots, 3$ for tricuspid valves) in image m is given by the intersection point corresponding to the smallest of the two minima. The centerlines, the centerline rays, their intersection points with the circular outline, and the anchor points are shown in Fig. 5(c).

The final anchor points $\mathbf{x}_{\mathrm{AP}_i}$ are determined by taking the mean (along the arc) of the corresponding anchor points for the 11 frames. This is shown in Fig. 5(d).

2) Snake initialization: The active contours need to be initialized after the valve starts to open and once enough orifice is visible. Initialization is done automatically, starting from the baselines of the leaflets. The initialization from the baseline has the additional advantage of placing snake point elements (often called snakels) already in the regions where the borders of the leaflets would otherwise be difficult to find because they are not well defined—they are imaged, e.g., against light parts of the tube seen through the orifice and are themselves bright [see Fig. 3(a)]. An example of the baseline initialization is shown in Fig. 4(a).

The snake tracks the outline of the leaflets only in images where this is well observable. Therefore, the initialization takes place only once the valve has wide opened sufficiently. We halt the snake at the end of the sequence when the opening is no longer large enough. The initialization from the baseline is done only relatively late after the valve has opened, such that the baselines fall in the attraction range of the leaflets. To determine when to initialize the snake, we extract the feature Υ, which is the mean of the gray levels $i(x, y)$ within the circle C inscribed in the triangle given by the base lines

$$\Upsilon = \frac{1}{N} \sum_{[x,y] \in C} i(x, y) \tag{5}$$

with N the number of pixels in C.

If the value of this feature is below a certain threshold t, we conclude that the valve has opened (o) and initialize the snake. At the end of the sequence, the snake-based tracking is halted as soon as the mean value is above the threshold, and we conclude that the valve has closed (c). We use the following decision rule:

$$\text{Decide } c \text{ if } \Upsilon > t; \text{otherwise, decide } o. \tag{6}$$

The threshold t is chosen as the median of the center mean values recorded over the first 25 frames of a sequence.

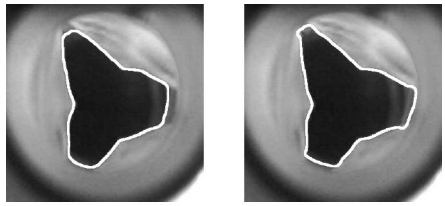

(a) (b)

Fig. 6. Segmentation of the orifice by active contours: (a) without and (b) and with attractor.

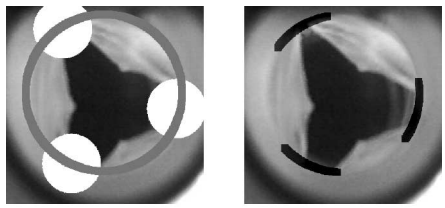

(a) (b)

Fig. 7. Construction of attractors: (a) dilated circular outline (in gray) with circular selection surfaces around each anchor point (in white) and (b) resulting semisynthetic image.

3) Snake-Based Tracking of Leaflet Border: After the snake has converged in the initialization frame, its position in the past image is used as initialization for the next one, etc.

During tracking, the snake cannot follow the valve orifice in regions of small contrast, i.e., where portions of the tube behind the valve are visible through the opening. This is shown in Fig. 6(a). We therefore introduce *attractors* for the snake around the anchor points such that the snake tracks the borders of the leaflets, as in the example shown in Fig. 6(b). By means of the attractors, we augment the standard snakes with explicit application-specific prior knowledge. While there are also other possibilities to formulate our problem within an active contours framework, such as the introduction of shape priors [5], [8], [16], the one proposed here, using attractors and anchor points that have an explicit physical meaning, is transparent to a user who may not be an expert in image processing, and provides marker points whose consistency with the heart valve can be checked at a glance.

To construct the attractors, we use the circular outline. The circular outline is first dilated slightly—by a disk structuring element with a radius of nine pixels—starting from its initial one pixel width, to increase its attraction range. Then, parts of the dilated outline O_{AP_j} around each anchor point $\mathbf{x}_{\mathrm{AP}_j}$ are selected. The selection includes those parts found in a circle of radius 125 pixels around each anchor point. The radius of the circle is related to the maximum distance between leaflets along the circular outline during the second phase of a valve cycle. This is shown in Fig. 7(a). Finally, the O_{AP_j} are subtracted

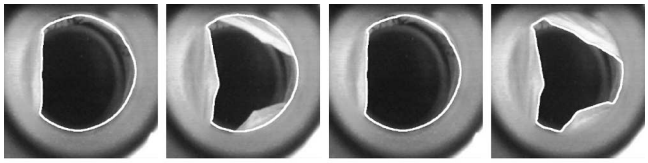

(a) (b) (c) (d)

Fig. 8. (a) and (b) Influence of the attractor's size on the snake results: snake-based orifice segmentation for two frames using the entire circular-outline as attractor. (c) and (d) Same images using only the portions of the circular outline around the anchor points as attractor.

from the original image $i(x, y)$ such that

$$E[i(x,y)|(x,y) \in O_{AP_j}] = D \tag{7}$$

for $j = 1, 2, 3$, with E the expectation operator estimated via the arithmetic mean and D the mean gray level value in the orifice. We thus obtain a semisynthetic image that is then used to compute the GVF. An example is shown in Fig. 7(b).

In (7), we use the mean gray level D in the orifice, such that the snake can leave the attractors under the influence of the internal energy term once the valve starts to close. The orifice gray levels are obtained from the unsupervised segmentation of the global histogram of the analyzed sequence. The global histogram includes the gray levels of the valve region as delineated by the circular outline in all frames of a test sequence [10].

We do not use the entire circular outline as one attractor because this may fail when one of the leaflets can no longer be observed when traveling outside the circular outline. The snake will then possibly remain there even when the valve starts closing. Such an example is shown in Fig. 8.

B. Orifice Curve

On a test sequence, the orifice curve is computed mainly by the snake, with the exception of some frames in the beginning and at the end of the sequence, and it is used to measure some quality criteria of the analyzed valve.

1) Quality Criteria Based on Orifice Curve: There are two quality criteria that can be measured from orifice curves. The first is the *maximum value* and the second is the *dynamic evolution* of the orifice area. For a healthy valve, the maximum value has to be within a certain predefined interval such that a proper blood flow is obtained under normal physiological heart cycle conditions. The dynamic evolution of a valve cycle has to exhibit *three phases* and the orifice curve of a healthy valve should accordingly show three regions. The first phase is the rapid increase phase, when the valve opens and the orifice area increases rapidly to its maximum value. During the second phase, the area of the orifice should decrease slowly, the valve being open now. Finally, in the third phase, the area decreases sharply, but with a smaller absolute slope than during the opening phase until the valve closes completely. This typical behavior is illustrated in Fig. 2.

The maximum value Ω of the valve orifice is read directly from the orifice curve and expressed in pixels. If the imaging geometry is known, the maximum value can be directly transformed into metric units. Equivalently, and to avoid the additional effort of calibrating the imaging geometry, we relate the maximum value as measured in pixels to the area A_{CO} enclosed by the circle describing the circular outline, which, as Fig. 5 shows, is computed for every sequence. As the absolute area corresponding to A_{CO} is fixed in our test bed, the ratio $\underline{\Omega} = \Omega / A_{\mathrm{CO}}$ is equivalent to calculating Ω in, say, centimeters square even when the imaging geometry should slightly change from valve to valve.

The dynamic behavior of the valve during the three phases Γ_i, $i = 1, \ldots, 3$, can be measured by a measure S_{Γ_i} that is based on the slope of the line interpolated from the orifice-curve values in each corresponding region. We describe how to segment the three orifice-curve regions corresponding to the three phases of the valve cycle in Section III-A1. S_{Γ_i} is computed as the normalized angle of the slope. The angle takes values in the interval $[-\pi/2, \pi/2]$. To obtain $S_{\Gamma_i} \in [-1, 1]$, the slope angle is normalized by $\pi/2$. Thus, the extreme case of a vertically increasing slope would have $S_{\Gamma_i} = 1$, a horizontal slope $S_{\Gamma_i} = 0$, and a vertically decreasing slope $S_{\Gamma_i} = -1$.

2) Practical Computation of Orifice Curves: To analyze an entire sequence, we use a global threshold to segment the orifice in those images at the beginning and the end of a sequence, where the snake cannot be properly defined. The global threshold is a fixed threshold, which remains the same for all images of the sequence. As shown in [4], this threshold is set on the global histogram by a likelihood ratio test, where the orifice and background gray level conditional probability density functions (pdfs) are estimated using mixture models [9].

One can be reasonably certain that a gray level threshold segments the orifice properly in the initial and end phases of the valve cycle, because it can be then safely assumed that the orifice—due to its small size—is imaged against an uniform background. Even though the thresholding method might fail in some rare cases, most of the sequence will still be correctly segmented by the snake, as the latter is initialized from the leaflet baseline and not from the thresholding result. The described combination between gray level threshold and snake successfully segments the orifice over an entire valve cycle.

III. Measuring Leaflet Fluttering

Without further physical experiments, we hypothesize from our data that there are two types of fluttering: *resonance fluttering* and *jerky fluttering*. Valves may exhibit both types of fluttering or any of the two alone. A good implant should not exhibit any jerky fluttering.

The effects of the fluttering can be observed in both time and space. Leaflets of a fluttering valve will exhibit a jerky motion, somewhat similar to a flag moving in the wind. At the same time, when they move during the second phase of a valve cycle, their borders will appear with an irregular form as they bend and wriggle in a plane approximately perpendicular to the image plane. An implant that exhibits such leaflet deformation is shown in Fig. 3(b).

The analysis of fluttering includes detection and quantification. Current fluttering measures, like the BDI, are space based as they assess how wriggled a leaflet is at a certain time instance.

Conversely, the human specialist takes into consideration both time and space aspects, when evaluating the fluttering of a valve, as he also observes the evolution of the valve's leaflets in the analyzed test sequence. We describe how to detect, and quantify the fluttering in the time domain on the orifice curves and in the space domain in each image. We also describe methods, which take into consideration information from both time and space and ultimately conclude, based on the results we have obtained that these represent the best way to measure the semantically important characteristics of fluttering.

A. Basics of Fluttering

Assuming that the leaflets are elastic, the flow of liquid through the valve is usually turbulent and can be thus modeled by a wideband noise signal that excites them. If the excitation signal also contains sufficiently large components of one of the resonance frequencies of the leaflets, these will start to vibrate as a whole without major changes along the borders of the leaflets, and the orifice will retain a neat star-like form [see Fig. 3(a)]. Such *resonance fluttering* has arguably a limited impact on the quality of a valve, as in this case while vibrating, and the leaflets move across their virtual baseline, i.e., the line connecting the two end points of a leaflet's border [see Fig. 4(a)], which is natural for them. The *jerky fluttering* is characteristic for valves with poor elastic properties, whose leaflets have no resonance frequencies. In this case, the leaflets also bend along lines perpendicular to the baseline [see, e.g., the right and the lower leaflet of the valve implant shown in Fig. 3(b)] and their borders, and hence, the borders of the orifice now appear wriggled. This type of fluttering causes major stress on the leaflets—thereby reducing the longtime durability of the implant—and influences the flow of blood strongly—with negative consequences for the health of the patient receiving the transplant. Jerky fluttering is thus a major issue in heart valve quality assessment [24].

We seek to quantify only jerky fluttering, which is, from now on, simply called fluttering, and we intend to measure fluttering for each leaflet. We measure fluttering only in the second phase of a valve cycle because, during opening and closing of the valve, the leaflets are tensed and do not flutter.

1) Segmentation of Second Phase of a Valve Cycle: The second phase of a valve cycle can be segmented using methods similar to those we developed earlier to analyze the inflow, presence, and outflow of contrast agent in sequences of coronary angiograms [1]. There, we have described how to segment a set of ordered observations $S = \{s_1, \ldots, s_n\}$ that increase in an initial phase, then remain approximately constant in an intermediary phase only to decrease in the final phase into three subsets: $\mathbf{s}_i, i = 1, 2, 3$, with $\bigcup_{j=1}^{3} \mathbf{s}_j = S$. The subsets correspond to two classes C_1 and C_2: C_1 represents the initial and final phases $\{\mathbf{s}_1, \mathbf{s}_3\}$, while C_2 represents the intermediary phase $\{\mathbf{s}_2\}$. Each observation receives a label $q_k \in \{C_1, C_2\}$, $k = 1, \ldots, n$. The set of orifice areas over the time axis during a valve cycle is also such an ordered set S and can be therefore segmented in the same way. Clearly, the second phase of a valve cycle corresponds to C_2.

A valid segmentation must provide a coherent second phase. A coherent second phase implies that it is unique and connected, with no "holes" in it. Holes appear when the succession of samples assigned to C_2 is interrupted by some C_1 samples followed by more C_2 samples. Assuming that the segmentation complies with the coherence condition, a small number of false positives means that there are few to none C_1 samples falsely assigned to C_2 only in the beginning and at the end of the second phase.

We seek the optimum segmentation subject to the maximum a posterior (MAP) criterion based on a two-state hidden Markov model (HMM) and subject to the aforementioned coherence constraint. Denoting the state sequence by $Q = \{q_1, \ldots, q_n\}$, we try to find Q such that $\Pr(Q|S)$ is maximized. The conditional pdfs of the observations conditioned on the states C_1 and C_2 are modeled by normal distributions. To estimate their parameters, the orifice curve is thresholded using Otsu's algorithm [21], such that separability between the classes is maximized. This global thresholding breaks the coherency constraint and thus it does not provide a valid segmentation; however, the result suffices to estimate the parameters of the pdfs. The sought coherence is reflected in a state transition matrix A, with the transition probabilities such that staying in the current state is strongly encouraged. Empirically, we have determined A to be

$$A = \begin{Bmatrix} 0.9 & 0.1 \\ 0.1 & 0.9 \end{Bmatrix}. \tag{8}$$

A consequence of the coherence constraint is that there are only $M = \binom{N}{2}$ different possibilities to segment a curve with N points into three coherent regions. As the typical length of an analyzed sequence is $N = 170$ [counting from the moment the valve starts to open and until it is completely closed, see Fig. 11(a)–(e)], there are only $M = 14\,365$ segmentation candidates to be tested by the MAP criterion. A full search over all valid segmentation results is therefore practically feasible. Results are shown in Fig. 11.

B. Fluttering Analysis in Time: Fluttering Measures Computed From Orifice Curve

A time-based analysis of fluttering seeks to quantify the "jerkiness" in the motion of the leaflets. The motion of the leaflets directly influences the area of the orifice, and hence fluttering can be measured on the orifice curves.

To conduct an analysis of the fluttering based on the orifice curves, we need to ensure that changes of the orifice area are generated only by the opening and closing of the valve. The snake-based approach practically fulfills this condition. Snake-based orifice curves reflect the true evolution of the orifice.

1) Detection of Fluttering: Fluttering causes the area of the orifice to change abruptly and often over time as the leaflets move erratically. Thus, fluttering can be detected on the orifice curves as a high-frequency signal superimposed on the portion of the curve corresponding to the second phase of a valve cycle (see the results in Fig. 11).

2) Quantification of Fluttering: After segmenting the second phase of a valve cycle, the 1-D signal $x_{oc}(t)$ given by the corresponding portion of the orifice curve is used to compute a measure of fluttering. For this purpose, we use the discrete Fourier transform (DFT). However, the DFT yields artifacts due to the assumed periodic repetition of the time signal. The artifacts are due to the trend present in $x_{oc}(t)$ as a consequence of the slowly decreasing orifice area during the second phase of a valve cycle. To eliminate them, we compensate for the trend before computing the DFT. The trend $\overline{x}_{oc}(t)$ is approximated by a second-order polynomial and then subtracted from $x_{oc}(t)$ to obtain the trend-free signal $\hat{x}_{oc}(t)$. The time-based fluttering measure denoted as Φ_{oc} is computed by the mean energy in the high-pass filtered $\hat{x}_{oc}(t)$

$$\Phi_{oc} = \frac{1}{2\pi}\left(\int_{-\pi}^{\pi} |\hat{X}_{oc}(\omega)|^2 d\omega - \int_{-\omega_{oc}}^{\omega_{oc}} |\hat{X}_{oc}(\omega)|^2 d\omega\right) \quad (9)$$

with $\hat{X}_{oc}(\omega)$ the Fourier transform of $\hat{x}_{oc}(t)$. The high pass eliminates frequency components related to low-frequency resonance fluttering. The band-edge frequency ω_{oc} is established empirically, as described in Section III-E. Experiments show that the more fluttering, the larger the measure.

C. Fluttering Analysis in Space: Fluttering Measures Based on Deformation of Leaflets

A space-based analysis of the fluttering seeks to measure the irregularity of the shape of the leaflets' borders. As shown in Section III-A, the irregularity of a leaflet border is related to flutter. The border of a leaflet is obtained directly by orifice area segmentation. The border of the orifice of a tricuspid heart valve usually exhibits three regions of relatively high curvature—one at each anchor point—not related to the fluttering; therefore, we need to analyze each leaflet alone. An additional reason for analyzing each leaflet alone is that we want to characterize each leaflet independently. For this purpose, we need to *segment the border of each leaflet* on the orifice border.

1) Segmentation of a Leaflet's Border: The valve orifice is defined by the borders of the leaflets that can be segmented on the orifice border. For this purpose, we use the anchor points that have already been computed. As the fluttering is analyzed only over the second phase of a valve cycle, i.e., when the orifice is large, these will be situated always on the border of the orifice and will thus define the borders of each leaflet. For a robust segmentation of the leaflets' borders, we use the anchor points together with the center of the valve to divide the image into three regions. These regions give then an implicit partition of the orifice border into curves corresponding to each leaflet. To make sure that the analysis concentrates only on leaflet borders and not on other artifacts—like the circular outline—after segmenting the leaflet border, we keep only the two-thirds around its center and ignore the rest [see Fig. 9(a) and (b)].

2) Detection and Quantification of Fluttering: An irregular border curve will contain relatively large amounts of energy in the high-frequency part of its spectrum. We therefore introduce a measure to quantify the irregularity of the border, which is related to the *energy* in the high-frequency part of the spectrum.

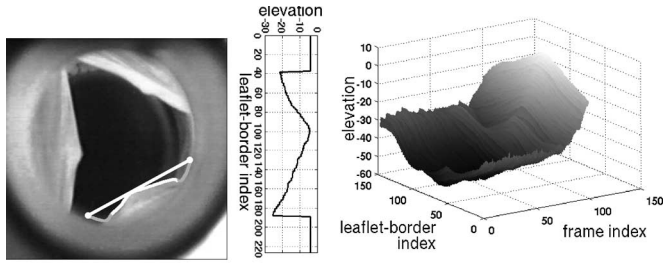

Fig. 9. Computation of time-space images. (a) Segmentation of the leaflet's border (in white and gray) over the baseline stretched between two anchor points and selection of the central part (in white). (b) Corresponding 1-D-signal obtained by sampling the leaflet's border over the baseline. (c) Time-space image obtained by gathering on the columns all sampled leaflet borders from the second phase of a valve cycle.

The measure is computed in each image acquired during the second phase of a valve cycle. We measure the fluttering for each leaflet by computing the mean of its measure over the entire sequence. The maximum over all leaflets then gives the fluttering for the analyzed valve.

a) Energy-based measure: We measure the fluttering by the high-frequency energy content of the 1-D signal $x_{bv}(t)$ given by the border of the leaflet. To analyze the fluttering alone, we first eliminate the DC component as well as the low-frequency part of the spectrum, which contains frequencies linked to the natural shape of the leaflet. The energy in the remaining components is the fluttering measure for the analyzed leaflet in a certain image of the test sequence.

The high-pass filtering takes place in the Fourier domain by setting to zero all spectral components up to the pass frequency ω_{bv}. The space-based fluttering measure denoted as Φ_{bv} is computed as follows:

$$\Phi_{bv} = \frac{1}{2\pi}\left(\int_{-\pi}^{\pi} |X_{bv}(\omega)|^2 d\omega - \int_{-\omega_{bv}}^{\omega_{bv}} |X_{bv}(\omega)|^2 d\omega\right) \quad (10)$$

with $X_{bv}(\omega)$ the Fourier transform of $x_{bv}(t)$. We choose ω_{bv} empirically, as described in Section III-E. Again, we use the DFT to compute the measure; however, due to the particular form of the leaflet, the artifacts introduced now usually have lower frequencies and are eliminated by the high-pass filter.

D. Fluttering Measure Computed From Time-Space Images

The fluttering is a time property of leaflets that is also related to the appearance of the leaflets' borders in each image, i.e., to space. We therefore measure here fluttering spatiotemporally. These measurements take place on each leaflet alone. The leaflets are segmented from the orifice, as described in Section III-C1.

1) Time-Space Images: To compute a time-space image, each leaflet-border curve is first sampled over the baseline linking the two corresponding anchor points [see Fig. 9(a)]. We then

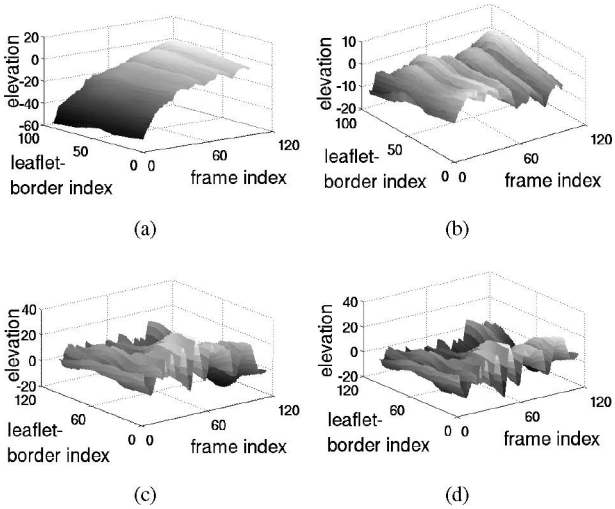

Fig. 10. Elimination of the trend present in the time space due to the natural tendency of a valve to close. (a) Time-space images of a nonfluttering leaflet, (b) trend-free times-space image of the same leaflet, (c) time-space images of a fluttering leaflet, and (d) its trend-free times-space image.

keep only two thirds of the leaflet measured over the baseline, thus obtaining for each image a 1-D signal of standard length [see Fig. 9(b)]. Finally, these signals taken from all images recorded during the second phase of a valve cycle are collected into the columns of a time-space image. An example is shown in Fig. 9(c).

Clearly, such images capture both the time evolution of the leaflets and the form of the leaflet border at each time instance. It also thus contains information about how the pattern of a leaflet's border changes in time and thus reflects the way a human observer would analyze the valve.

2) Measure of Fluttering: The time-space fluttering measure for a leaflet, denoted as Φ_{ts}, is related to the mean high-pass energy in such time-space images $i_{ts}(x,y)$. The maximum over all leaflets then yields a fluttering measure for an entire sequence.

The computation of Φ_{ts} is done in the frequency domain by the DFT. Similar to the case of the time-based fluttering measure in Section III-B, we also have high-frequency artifacts due to the trend introduced in the time-space images by the natural tendency of the valve to close during the second phase of a valve cycle. This trend is easily observable in time-space images of good leaflets. The example in Fig. 10(a) clearly shows such a trend.

The trend-related artifacts have a negative influence on our measure and decrease its sensitivity. To compensate for this, we estimate the trend and subtract it from the analyzed images. For this purpose, we take the spatial mean in the time-space images and thus obtain a time-varying curve whose values we approximate by a second-order polynomial. We then build $\bar{i}_{ts}(x,y)$ by repeating along the space axis the values the polynomial takes at the respective time instance. A trend-free time-space image is obtained as $\tilde{i}_{ts}(x,y) = i_{ts}(x,y) - \bar{i}_{ts}(x,y)$. Fig. 10(b) and (d) shows two examples.

TABLE I
TEST SEQUENCES IN DATABASE

Sequence	Fluttering	Observations
A	no	resonance fluttering of low amplitude and high frequency
B	strong	no resonance fluttering observable
C	low	resonance fluttering of low amplitude and high frequency; stronger fluttering for one leaflet
D	strong	no resonance fluttering observable
E	low	resonance fluttering of high amplitude and low frequency

Φ_{ts} is computed from $\tilde{i}_{ts}(x,y)$ by high-pass filtering

$$\Phi_{ts} = \frac{1}{4\pi^2}\int_{-\pi}^{\pi}\int_{-\pi}^{\pi} |\tilde{I}_{ts}(\omega_1,\omega_2)|^2 d\omega_1 d\omega_2 - \frac{1}{4\pi^2}\int_{-\omega_{ts_1}}^{\omega_{ts_1}}\int_{-\omega_{ts_2}}^{\omega_{ts_2}} |\tilde{I}_{ts}(\omega_1,\omega_2))|^2 d\omega_1 d\omega_2 \quad (11)$$

with $\tilde{I}_{ts}((\omega_1,\omega_2))$ the Fourier transform of $\tilde{i}_{ts}(x,y)$. The pass frequencies of the high-pass filter ω_{ts_1} and ω_{ts_2} are empirically set for both dimensions, as described in Section III-E. The high-pass filter then eliminates the low-frequency resonance vibration and the low-frequency components introduced by the natural shape of a leaflet.

E. Parameter Selection for Measuring Fluttering

Irrespective of the approach used, the fluttering is measured as the energy of a signal in the high-pass part of its spectrum. For this purpose, we use high-pass filters whose band edges are established empirically, using as ground truth a set of sequences obtained from valves whose fluttering characteristics were known beforehand. The band edges for each of the proposed fluttering estimators were modified until we obtained measurements that reflected our qualitative prior knowledge on the fluttering behavior of the ground truth sequences. Toward this end, the sequences were graded from 0 to 1, with one standing for the largest fluttering. We then computed for each band edge—in an interval from 0 to $\pi/2$—and for every sequence, our respective fluttering measure and scaled the results to $[0,1]$. Finally, we computed the mean square error between the grades and the measures. The band edges proposed are those for which this error was minimal. The following parameters were found as optimal: $\omega_{oc} = \pi/4$ in (9), $\omega_{bv} = \pi/10$ in (10), and $\omega_{ts_1} = \omega_{ts_2} = \pi/20$ in (11).

IV. EXPERIMENTS AND DISCUSSION

We have tested the algorithms proposed here on five test sequences chosen such that they cover—to the best of our knowledge to date—the entire spectrum of problems encountered when analyzing valves. All sequences show valves with three leaflets. They represent our ground truth reference and are described in Table I. The fluttering labels were assigned by a human expert.

A test sequence has usually some 170 frames and can go up to 250 frames. For such data, we obtain a complete set of

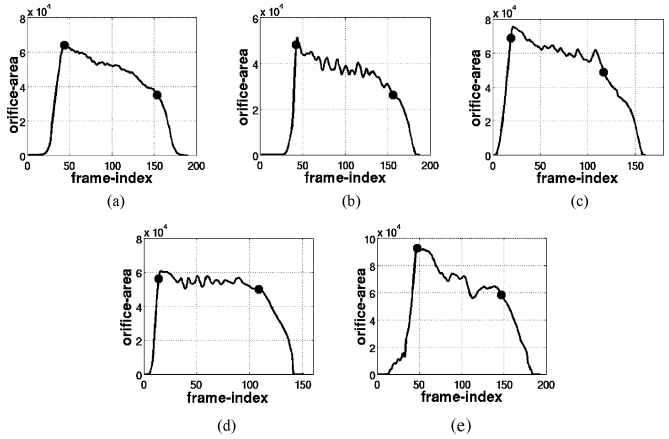

Fig. 11. Orifice curves computed using snakes. The dots mark the beginning and end of the second phase of a valve cycle.

TABLE II
MAXIMUM VALUE OF ORIFICE Ω MEASURED IN PIXELS, MAXIMUM RELATIVE TO CIRCULAR OUTLINE $\underline{\Omega}$, AND NORMALIZED SLOPE ANGLE S_Γ IN EACH OF THREE CURVE REGIONS Γ_i, $i = 1, \ldots, 3$, FOR SEQUENCES IN DATABASE

Sequence	Ω	$\underline{\Omega}$	S_{Γ_1}	S_{Γ_2}	S_{Γ_3}
A	64028	0.96	0.91	-0.33	-0.83
B	51233	0.72	0.91	-0.25	-0.81
C	75336	0.82	0.93	-0.22	-0.70
D	60824	0.68	0.95	-0.10	-0.81
E	92733	0.95	0.88	-0.35	-0.78

measurements after approximately 25 min under MATLAB on a P4 machine running at 2.3 GHz.

A. Measurements Related to Orifice Area

The orifice area is obtained as the area enclosed by the snake and its edge is directly obtained from the snake. Fig. 11 shows orifice curves for each of the sequences in the database. These orifice curves correspond to the expectations of a human expert.

The result of the segmentation depends on the attraction range of the external energy and also on the way the energy is defined around the anchor points. The attractors make sure that the external energy field converges properly there. A GVF offers a large attraction range and a good convergence in regions of high border curvature [27]. Moreover, since the images are acquired at high frame rate, the distance traveled by the leaflets between two consecutive images is small enough such that the converged snake from the previous image is practically always in the attraction sink of the leaflet borders in the current image. On the tested sequences, the snake was robust enough to always track the borders. Should the snake fail, one may improve the segmentation by going backward on the time axis, as the processing is done offline.

The results for the valves examined are given in Table II. The second and third columns show the maximum value of the orifice area in pixels as well as the normalized maximum value, while the last three columns show the relative angles of the slopes of the orifice curves in each of the three regions, as described in Section II-B1. To make this measure independent of the maximum value, the values of each orifice curve were first normalized to the interval $[0, 1]$. They correlate well with the orifice area curves, showing a steep increase in the first region Γ_1, a slow decrease during Γ_2, and a steep decrease during Γ_3.

TABLE III
FLUTTERING MEASURED BY DIFFERENT METHODS FOR SEQUENCES IN OUR DATABASE

Seq.	Time based	Space based			Time-space based		
	$\underline{\Phi}_{oc}$	$\underline{\Phi}_{bv_1}$	$\underline{\Phi}_{bv_2}$	$\underline{\Phi}_{bv_3}$	$\underline{\Phi}_{ts_1}$	$\underline{\Phi}_{ts_2}$	$\underline{\Phi}_{ts_3}$
A	0.328	0.023	0.043	0.032	0.017	0.073	0.012
B	0.582	0.047	0.152	0.319	0.206	0.204	0.256
C	0.472	0.048	0.071	0.025	0.039	0.119	0.041
D	0.572	0.062	0.104	0.188	0.245	0.172	0.330
E	0.478	0.035	0.061	0.037	0.071	0.190	0.100

The measures were normalized such that one corresponds to the extreme fluttering of a hypothetical reference valve (see text).

B. Fluttering Detection and Quantification

Fluttering is analyzed only during the second phase of a valve cycle, i.e., for sequence A, between frames 42 and 152, for sequence B between frames 41 and 158, for sequence C between frames 18 and 117, for sequence D between frames 15 and 113, and for sequence E between frames 47 and 143.

In Section III, we have described three approaches to detect and quantify fluttering. The results obtained by each of them are shown in Table III. They are normalized to the interval $[0, 1]$ with one corresponding to a valve characterized by extremely strong fluttering. This worst case valve is a hypothetical reference model, whose leaflets are all identical and exhibit a BDI of 0.95. The worst natural valves do not exceed a BDI of 0.8 [7], [20]. In the time domain, each leaflet of the worst case valve flutters at 60 Hz. This corresponds to some 15 oscillations during the second phase of a valve cycle, with an amplitude comparable to that of a natural valve. Also, the length of the border of a leaflet is comparable to that of a natural leaflet. For the worst-case valve, $\Phi_{oc} = 466$, $\Phi_{bv_i} = 5812$, and $\Phi_{ts_i} = 1786 \times 10^3$ with $i = 1, 2, 3$.

The simplest and fastest way to measure fluttering for an entire sequence is by a frequency analysis of the orifice curves. As shown in Table III, the results achieved by the time-based measure correlate well with the test-sequence properties referenced in Table I. However, there is no possibility to measure the fluttering of each leaflet of the valve.

Practically, a contorted border shape which varies in time is an indication of fluttering for the respective valve. Thus, the shape of the leaflet's border is related to fluttering. However, one could theoretically observe a valve whose leaflets' borders have a contorted shape, but this shape does not change in time. Such a valve is not considered to flutter.

The space-based measure returns results that do correlate with the ground truth. This may be also seen as a confirmation of the fact that in the sequences from our database, an irregular pattern of the border of a leaflet implies that the leaflet flutters. In this case, each leaflet can be measured, but one cannot differentiate between valves that maintain the pattern of their borders and those that do not.

Time-space images can be used to characterize both the time and space evolution of a leaflet, and therefore can additionally

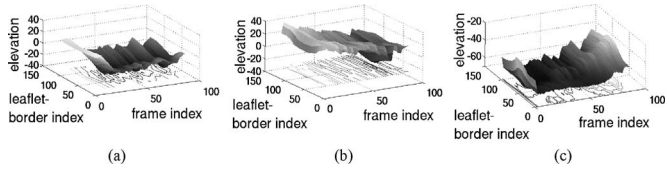

Fig. 12. Time-space image for the three leaflets of sequence C with the corresponding fluttering measure (F). (a) $F = 0.039$. (b) $F = 0.119$. (c) $F = 0.041$.

differentiate between valves that keep the pattern of their borders and those that do not. An example is shown in Fig. 12. These results do correlate very well with the test-sequence properties referenced in Table I. Measures based on time-space images reflect the way a human expert would evaluate the fluttering of a valve, i.e., by taking into consideration both time and space aspects.

All methods proposed here return results, which are in agreement with our ground truth. Resonance fluttering can be measured mainly by time-related measures. As it can be seen from Table I, valves with low to no flutter usually exhibit high-frequency resonance fluttering, but of very low amplitude, such that they do not influence neither the time-based nor the time-space-based fluttering measures practically.

Time-based measures are fast to compute, but they cannot return information for each leaflet alone. Space-based measures, on the other hand, measure only a consequence of the fluttering, namely, the irregular shape of the border of the leaflets. A time-space image offers the most information on all aspects of fluttering and can also be computed for each leaflet alone. Therefore, we conclude that measuring the fluttering by means of time-space images is the best way, as it offers the largest amount of information and thus enables an improved analysis in comparison to the other methods.

V. Conclusion

We have described methods for the automatic computation of quality measures for heart valves. The input image sequences are acquired by a specially designed test bed that emulates physiological blood flow. These image sequences show one entire valve cycle from the moment the valve opens until it closes. While current manual analysis of these image data only focuses on measuring the maximum orifice area, our approach additionally captures the dynamic behavior of the orifice area during the entire valve cycle, and summarizes this into three measures characterizing the valve opening phase, the open phase, and the closing phase. Moreover, while currently, the phenomenon of leaflet fluttering is mainly assessed visually, we have also provided criteria to assess fluttering, with the time-space based methods being most meaningful. These criteria are normalized by a hypothetical reference valve that exhibits an extreme amount of fluttering. In addition to making the assessment of heart valves faster, more precise, and more reproducible, our approach also describes the valves more comprehensively than the current manual method. We have so far validated our algorithms on five sequences. As the image data are acquired in the carefully controlled test bed environment, we do not expect the quality of the orifice segmentation results to vary significantly when more data become available. Currently, our algorithms and criteria are being applied in medical routine. We will report on more validation results as well as potential refinement of the parameters, such as the band edges of the high-pass filters, in the near future. Another possibility—suggested by one reviewer—to further develop this method is to evaluate several valve cycles, rather than only one, and to average the resulting measurements over the cycles.

As of now, we have applied these methods to assess the quality of heart valves with three leaflets. This category includes the aortic, the pulmonary, and the tricuspid valves. However, we believe that these methods can also be used for bicuspid valves, thus constituting a tool for heart valve analysis in general.

References

[1] T. Aach, A. P. Condurache, K. Eck, and J. Bredno, "Statistical-model based identification of complete vessel-tree frames in coronary angiograms," in *Electronic Imaging 2004: Computational Imaging II*, vol. 5299, San Jose, CA: SPIE, 2004, pp. 283–294.

[2] J. Canny, "A computational approach to edge detection," *IEEE Trans. Pattern Anal. Mach. Intell.*, vol. PAMI-8, no. 6, pp. 679–698, Jan. 1986.

[3] V. Caselles, R. Kimmel, and G. Sapiro, "Geodesic active contours," *Int. J. Comput. Vis.*, vol. 22, no. 1, pp. 61–79, 1997.

[4] A. P. Condurache, T. Hahn, U. G. Hofmann, M. Scharfschwerdt, M. Misfeld, and T. Aach, "Automatic measuring of quality criteria for heart valves,," in *Medical Imaging 2007: Image Processing*, vol. 6512, San Diego, CA: SPIE, 2007, pp. 2Q1–2Q11.

[5] D. Cremers, F. Tischhäuser, J. Weickert, and C. Schnörr, "Diffusion snakes: Introducing statistical shape knowledge into the mumford-shah functional," *Int. J. Comput. Vis.*, vol. 50, no. 3, pp. 295–313, 2002.

[6] T. E. David, "Aortic valve replacement with stentless porcine bioprostheses," *J. Card. Surg.*, vol. 13, no. 5, pp. 344–351, 1998.

[7] A. Erasmi, H.-H. Sievers, M. Scharfschwerdt, T. Eckel, and M. Misfeld, "In vitro hydrodynamics, cusp-bending deformation, and root distensibility for different types of aortic valve-sparing operations: Remodeling, sinus prosthesis, and reimplantation," *Thorac. Cardiovasc. Surg.*, vol. 130, no. 4, pp. 1044–1049, 2005.

[8] W. Fang and K. L. Chan, "Incorporating shape prior into geodesic active contours for detecting partially occluded object," *Pattern Recognit.*, vol. 40, no. 8, pp. 2163–2172, 2007.

[9] M. A. T. Figueiredo and A. K. Jain, "Unsupervised learning of finite mixture models," *IEEE Trans. Pattern Anal. Mach. Intell.*, vol. 24, no. 3, pp. 381–396, Mar. 2002.

[10] T. Hahn, A. P. Condurache, T. Aach, M. Scharfschwerdt, and M. Misfeld, "Automatic in-vitro orifice area determination and fluttering analysis for tricuspid heart-valves," in *Proc. BVM-2006*. Hamburg, Germany: Springer-Verlag, 2006, pp. 21–25.

[11] P. V. C. Hough, "Methods and means for recognizing complex patterns,,", U.S.Patent 3 069 654, 1962.

[12] J. Illingworth and J. Kittler, "A survey of the Hough transform," *Comput. Vis. Graph. Image Process.*, vol. 44, no. 1, pp. 87–116, 1988.

[13] B. Jähne, *Image Processing for Scientific Applications*. Boca Raton, FL: CRC Press, 1997.

[14] A. K. Jain, Y. Zhong, and M.-P. Dubuisson-Jolly, "Deformable template models: A review," *Signal Process.*, vol. 71, no. 2, pp. 109–129, 1998.

[15] M. Kass, A. Witkin, and D. Terzopoulos, "Snakes: Active contour models," *Int. J. Comput. Vis.*, vol. 1, no. 4, pp. 321–331, 1988.

[16] O. F. M. E. Leventon and W. E. L. Grimson, "Statistical shape influence in geodesic active contours," in *Proc. CVPR-2000*, Jun.13–15,, vol. 1, pp. 1316–1321.

[17] R. Malladi, J. A. Sethian, and B. C. Vemuri, "Shape modelling with front propagation: A level set approach," *IEEE Trans. Pattern Anal. Mach. Intell.*, vol. 17, no. 2, pp. 158–175, Feb. 1995.

[18] T. McInerney and D. Terzopoulos, "Deformable models in medical images analysis: A survey," *Med. Image Anal.*, vol. 1, no. 2, pp. 91–108, 1996.

[19] Z. Nagy, J. Fisher, P. Walker, and K. Watterson, "The effect of sizing on the in vitro hydrodynamic characteristics and leaflet motion on the Toronto SPV stentless valve," *Thorac. Cardiovasc. Surg.*, vol. 117, no. 1, pp. 92–98, 1999.

[20] Z. Nagy, J. Fisher, P. Walker, and K. Watterson, "The effect of sizing on the hydrodynamic parameters of the medtronic freestyle valve *in vitro*," *Ann. Thorac. Surg.*, vol. 69, no. 1, pp. 1408–1413, 2000.
[21] N. Otsu, "A threshold selection method from gray-level histograms," *IEEE Trans. Syst., Man Cybern.*, vol. SMC-9, no. 1, pp. 62–66, Jan. 1979.
[22] N. Ray and S. T. Acton, "Data acceptance for automated leukocyte tracking through segmentation of spatiotemporal images," *IEEE Trans. Biomed. Eng.*, vol. 52, no. 10, pp. 1702–1712, Oct. 2005.
[23] M. Scharfschwerdt, M. Misfeld, and H.-H. Sievers, "The influence of a nonlinear resistance element upon in-vitro aortic pressure tracings and aortic valve motions," *Amer. Soc. Artif. Intern. Organs*, vol. 50, no. 5, pp. 498–502, 2004.
[24] T. Vesely, D. Boughner, and T. Song, "Tissue buckling as a mechanism of bioprosthetic valve failure," *Ann. Thorac. Surg.*, vol. 46, no. 3, pp. 302–308, 1988.
[25] W. Vongpatanasin, L. D. Hillis, and R. A. Lange, "Prosthetic heart valves," *Med. Prog.*, vol. 355, no. 6, pp. 407–416, 1996.
[26] W. Vongpatanasin, L. D. Hillis, and R. A. Lange, "Generalized gradient vector flow external forces for active contours," *Signal Process.*, vol. 71, no. 2, pp. 131–139, 1998.
[27] C. Xu and J. L. Prince, "Snakes, shapes, and gradient vector flow," *IEEE Trans. Image Process.*, vol. 7, no. 3, pp. 359–369, Mar. 1998.
[28] J. Xu, O. Chutatape, and P. Chew, "Automated optic disk boundary detection by modified active contour model," *IEEE Trans. Biomed. Eng.*, vol. 54, no. 3, pp. 473–482, Mar. 2007.

Alexandru Paul Condurache received the Dipl.-Ing. degree in electrical engineering and the Diploma of Advanced Studies in biomedical engineering from the Politehnica University of Bucharest, Bucharest, Romania, in 2000 and 2002, respectively, and the Dr.-Ing. degree in computer science from the University of Luebeck, Luebeck, Germany, in 2007.

Since 2002, he has been with the Institute for Signal Processing, University of Luebeck, as a Research Associate, where he was in charge of several projects in the field of medical image analysis and industrial machine vision. His current research interests include machine vision applications in biomedical engineering and in industry, image analysis, event detection, and discriminant-feature analysis.

Tobias Hahn was born in Luebeck, Germany, on August 14, 1975. He received the Diplom-Informatiker degree (equivalent to M.Sc. degree in computer science) from the University of Luebeck, Luebeck, Germany, in 2006.

He was involved in the field of image processing. He was a student assistant with the Institute for Signal Processing, University of Luebeck, where he contributed algorithms to several image processing projects. He was also involved in image-based methods for the automatic inspection of heart valves. He is currently with the Department for Software Quality Assurance, Siemens Medical Solutions, Erlangen, Germany.

Michael Scharfschwerdt was born in Luebeck, Germany, on November 28, 1962. He received the Dipl.-Ing.(FH) degree in mechanical engineering in 1989 and the Dipl.-Ing.(FH) degree in Biomedical Technologies in 2003 both from the University of Applied Sciences Luebeck, Luebeck.

Between 1994 and 2001, he was with the Laboratory for Biomedical Technologies, University of Applied Sciences Luebeck. He is currently with the Clinic for Heart Surgery, University Clinic Schleswig-Holstein, Luebeck, where he is involved in research related to the hydrodynamical modeling of the heart.

Alfred Mertins (M'96–SM'03) received the Dipl.-Ing. degree from the University of Paderborn, Paderborn, Germany, in 1984, and the Dr.-Ing. degree in electrical engineering and the Dr.-Ing. Habilitation degree in telecommunications from Hamburg University of Technology, Hamburg, Germany, in 1991 and 1994, respectively.

From 1986 to 1991, he was a Research Assistant at Hamburg University of Technology. From 1991 to 1995, he was a Senior Scientist at Microelectronics Applications Center Hamburg, Germany. From 1996 to 1997, he was with the University of Kiel, Germany, and from 1997 to 1998, he was with the University of Western Australia. In 1998, he joined the University of Wollongong, where he was an Associate Professor of electrical engineering. From 2003 to 2006, he was a Professor in the Faculty of Mathematics and Science, University of Oldenburg, Germany. In November 2006, he joined the University of Luebeck, Germany, where he is currently a Professor and the Director of the Institute for Signal Processing. His research interests include speech, audio, and image processing, wavelets and filter banks, pattern recognition, and digital communications.

Til Aach (M'94–SM'02) received the Diploma and Doctoral degrees in electrical engineering from Rheinisch-Westfaelische Technische Hochschule (RWTH) Aachen University, Aachen, Germany, in 1987 and 1993, respectively.

He was a Research Scientist with the Institute for Communications Engineering, RWTH Aachen University, where he was in charge of several projects in image analysis, 3-D-television, and medical image processing. From 1993 to 1998, he was with Philips Research Labs, Aachen, Germany, where he was responsible for several projects in medical imaging, image processing and analysis. During 1996, he was also an independent Lecturer with the University of Magdeburg, Germany. In 1998, he was appointed a Full Professor and Director of the Institute for Signal Processing, University of Luebeck. In 2004, he became the Director of the Institute of Imaging and Computer Vision, RWTH Aachen University. His current research interests include medical and industrial image processing, signal processing, pattern recognition, and computer vision. He has authored or co-authored more than 250 papers. He is a co-inventor for about 20 patents.

Prof. Aach is an Associate Editor of the IEEE TRANSACTIONS ON IMAGE PROCESSING. He is a member of the Bio-Imaging and Signal Processing Committee of the IEEE Signal Processing Society. He was the Technical Program Co-Chair for the IEEE Southwest Symposium on Image Analysis and Interpretation in 2000, 2002, 2004, and 2006. He was the recipient of several awards, including German Informationstechnische Gesellschaft (ITG/VDE) for a paper published in the IEEE TRANSACTIONS ON IMAGE PROCESSING in 1998.